Experiments in Fluids (2006) 41: 343–352
DOI 10.1007/s00348-006-0142-9

RESEARCH ARTICLE

Y. Murai · Y. Oishi · Y. Takeda · F. Yamamoto

Turbulent shear stress profiles in a bubbly channel flow assessed by particle tracking velocimetry

Received: 15 November 2005 / Revised: 18 March 2006 / Accepted: 20 March 2006 / Published online: 26 April 2006

Abstract Particle tracking velocimetry (PTV) is applied to a bubbly two-phase turbulent flow in a horizontal channel at $Re = 2 \times 10^4$ to investigate the turbulent shear stress profile which had been altered by the presence of bubbles. Streamwise and vertical velocity components of liquid phase are obtained using a shallow focus imaging method under backlight photography. The size of bubbles injected through a porous plate in the channel ranged from 0.3 to 1.5 mm diameter, and the bubbles show a significant backward slip velocity relative to liquid flow. After bubbles and tracer particles are identified by binarizing the image, velocity of each phase and void fraction are profiled in a downstream region. The turbulent shear stress, which consists of three components in the bubbly two-phase flow, is computed by analysis of PTV data. The result shows that the fluctuation correlation between local void fraction and vertical liquid velocity provides a negative shear stress component which promotes frictional drag reduction in the bubbly two-phase layer. The paper also deals with the source of the negative shear stress considering bubble's relative motion to liquid.

1 Introduction

The use of bubbles as a way of reducing skin frictional drag in turbulent flows has become a focus for engineers in the expectation that it might be applicable to ships and pipelines. Depending upon the bubbles' size, there are two main methodologies. One is the so-called microbubble method, first reported by McCormick and Bhattacharyya (1973). They employed electrolysis to generate microbubbles in water and were able to demonstrate some degree of drag reduction for a submersible hull. Another is the so-called air film method (e.g., Fukuda et al. 2000). The air film method simply cuts off contact between the water and wall surface. Therefore, the technical problem is how to maintain a stable air sheet on the target wall. Considering the gain factor in drag reduction, which is the drag-reducing ratio per void fraction in the boundary layer, the microbubble method is recognized as more effective than the air film method as a power-saving technique. In fact the gain factor of the microbubble method, being calculated from the data in published papers (e.g., Kato et al. 1999), ranges usually from 2 to 10, implying a very high sensitivity of the bubbles in altering the structure of the boundary layer. The use of bubbles whose size is comparable to the thickness of boundary layer leads to a drag increment, i.e. a negative gain factor (Fukuda et al. 2005).

Ascertaining the mechanism of such a very effective drag reduction using small bubbles, laboratory experiments using water tunnels or channels have been carried out by a number of researchers (Madavan et al. 1985; Merkle and Deutsch 1992; Kodama et al. 2000; Moriguchi and Kato 2002; Gabillet et al. 2002). Characterization of the fundamental effect of bubbles has been published by Legner (1984) and Marie (1987), with reference to such aspects as the reduction in density of the mixture, and modification of the effective viscosity inside the boundary layer. Numerical researches dealing with small spherical bubbles were reported by Felton and Loth (2002), Xu et al. (2002), Kawamura and Kodama (2002), and Ferrante and Elghobashi (2004), and elaborated on the process of microbubble drag reduction. Tests of the application of small bubbles to ships or long flat plates were reported by Takahashi et al. (2003) and Latorre et al. (2003). After considering numerous sets of published experimental data, we conclude that not only

Y. Murai (✉) · Y. Oishi · Y. Takeda
Division of Energy and Environmental System,
School of Engineering, Hokkaido University,
Sapporo 060-8628, Japan
E-mail: murai@eng.hokudai.ac.jp
Tel.: +81-11-7066372
Fax: +81-11-7067889

F. Yamamoto
Fiber Amenity Engineering Course,
School of Engineering, University of Fukui, Fukui, Japan

"real microbubbles" but also "a-few-millimeter bubbles" can reduce skin friction, as reported by Moriguchi and Kato (2002). They found that there appears to be no significant bubble size dependency in conditions of high shear rate. With these findings, the recent discussion has moved to the role of the bubble's deformability in reducing the local Reynolds shear stress, as reported by Kitagawa et al. (2005). Lu et al. (2005) numerically confirmed such a positive role of bubble's deformability in drag reduction recently. In this context, the bubbles are not required to be so small in size or Weber number. In other words, a mechanism of drag reduction, independent of that involving spherical bubbles, may take place after the bubbles start to deform.

In our experiments, particle tracking velocimetry (PTV) was applied to a bubbly two-phase turbulent flow in a horizontal channel at $Re = 2 \times 10^4$. The size of the bubbles injected through a porous plate in the channel range from 0.3 to 1.5 mm in diameter, and the bubbles have a significant relative velocity to liquid flow (i.e. non-homogeneous bubbly flow). Bubbles and tracer particles are photographed using a shallow focus imaging method that does not require laser sheet illumination. After bubbles and tracer particles were identified by binarizing the images, the velocity of each phase and void fraction are profiled in a downstream region. In one of the new trials to extract the drag reduction mechanism, three kinds of turbulent shear stresses are derived from the momentum conservation equation of two-phase flow, and are computed using the present set of PTV data. Bubble's motion in the shear layer in relation to the modification of turbulent shear stress is also discussed using a simple theory of bubble's translational motion.

2 Experimental method

2.1 Test facility

A schematic diagram of the experimental apparatus is shown in Fig. 1. The test section is a horizontal rectangular channel made of transparent acrylic resin, which is 100 mm in width, 10 mm in height, and 6,000 mm in length. Water and air are used as liquid and gas phases under laboratory temperature (13–16 °C). Water circulates through a tank, a pump, a flowmeter, a diverging–converging channel, and the test horizontal channel, which includes a bubble injector in the upstream part. Bubbles are completely removed inside the tank before the liquid flows out and returns to the channel. This bubble removal operation is provided by a double chamber structure of the tank in which swirling effect in the inner chamber and buoyant separation effect in the outer chamber are utilized.

The outline of bubble injection device is shown in Fig. 2. Air bubbles are injected into the horizontal channel from the top inner surface of the channel, through a porous plate made of alumina with a nominal pore diameter of approximately 60 μm and injection area of 88 × 14 mm. The injector is located at 875 mm downstream of the end of the diverging–converging section or inlet of the channel. Water is not purified or distilled, because small solid tracer particles are seeded for implementing PTV. Therefore, the air bubble behaves as contaminated bubble in the present experiment.

The mean flow speed of liquid in the cross section is $U = 2.0$ m/s corresponding to $Re = 2 \times 10^4$ (here Re number is defined by $Re = 2Uh/\nu$ where h is half the height of the channel, and ν the kinematic viscosity of liquid). Detailed experimental conditions are summarized in Table 1.

2.2 Qualitative visualization

Typical pictures of near-wall turbulence affected by bubbles are shown in Fig. 3. These are visualized using a Kalliroscope (AQ1000, Kalliroscope Co. Ltd.), which can detect local shearing and rotating structures of the turbulence by the optical property of the flake-like glossy particles. The detail of the Kalliroscope for fluid flow visualization is summarized in the paper of Dominguez-Lerma et al. (1985), who investigated a Taylor–Couette flow. In our visualization, a horizontal sheet of

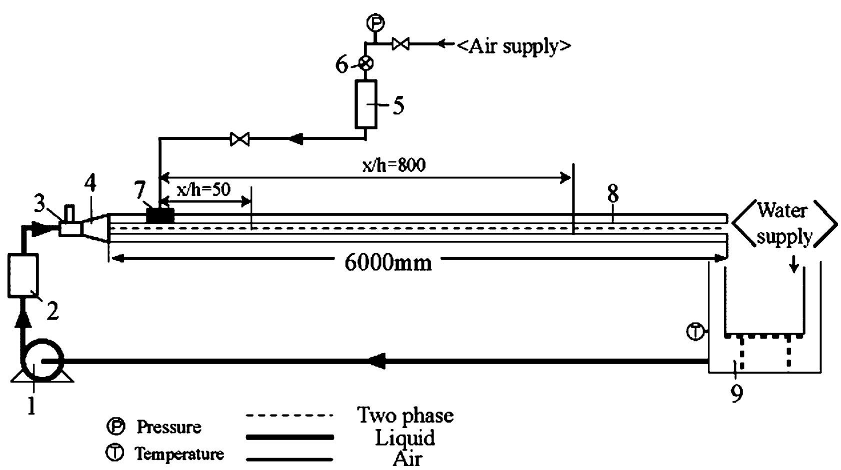

Fig. 1 Schematic diagram of the experimental apparatus. *1* Pump, *2* chamber, *3* water flowmeter, *4* diverging-converting channel, *5* air flowmeter, *6* regulator, *7* bubble injector device, *8* rectangular channel (test section), *9* bubble removable tank

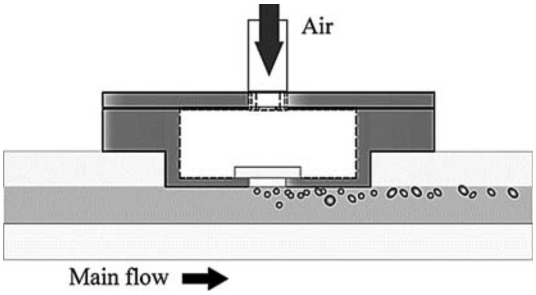

Fig. 2 The bubble injector device using porous plate

light with a thickness of around 3 mm was projected near the upper wall of the channel. With this illumination, streamwise vortices reflect the light to the camera located above the channel so that those distributions in the x–z plane inside the boundary layer are identified by white stripes. In the case of the single-phase condition, a number of streamwise vortices occur in the 100 × 30 mm viewing area, as shown in Fig. 3a. As bubbles larger than 20 mm are mixed, this structure disappears inside individual bubbles, but it remains intact in the liquid phase (see Fig. 3b). This alternation qualitatively corresponds to the hypothesis of air film-base drag reduction, in which the frictional drag is reduced in proportion to the ratio of bubble-covering area to the wall surface area (Fukuda et al. 2000). In comparison to the latter, small bubbles effectively restrict the production of small eddies in the liquid phase as well (see Fig. 3c). This change may relate strongly to a reduction of the Reynolds shear stress. One apparent fact is that the representative spanwise wavelength of the streamwise vortices (which is around 3 mm in the single-phase condition) is in the same order of bubble spacing in the case of small bubble mixture. Therefore, the bubble and the eddy must show a strong interaction to each other, which drastically modifies the structure of the boundary layer. This is the background of this study, as well as our motivation for progressing towards a quantitative visualization using PTV.

Table 1 Experimental conditions

Channel size	10 mm × 100 mm × 6,000 mm
Channel half height	h = 5 (mm)
Bulk void fraction	α = 0.08 (%)
Mean bubble diameter	D = 0.7 (mm)
Bulk liquid velocity	U = 2.0 (m/s)
Bulk Reynolds number, $Re = 2hU/\nu$	2×10^4
Frictional Reynolds number, $Re_\tau = hu_\tau/\nu$	550
Measurement point	x/h = 50, 800
Frame rate	4,000 (fps)
Shutter speed	$1/1.5 \times 10^5$ (s)
Resolution	1,024 × 512 (pixels)
Sampling time	T = 0.2 (s)
Sampling velocity number	1×10^6

2.3 Quantitative visualization method

Particle tracking velocimetry is used to measure the liquid flow structure in the bubbly two-phase flow. PIV based on image cross correlation is intentionally avoided in order to distinguish the two phases, and to detect turbulence accurately. Tracer particles seeded in the water loop are of a porous type of plastic polymer particle (Hyporous polymer particles, Dyaion Co. Ltd.), which is 1,020 kg/m^3 in effective density and 30 μm in mean diameter in immersed state. As illustrated in Fig. 4, a metal halide light of 250 W is projected in a horizontal spanwise direction, while the camera is located on the backside, i.e. backlight photography. Tracer particles and the bubble interface are projected as dark shadows on the image. The focal plane is adjusted on the central plane of the channel,

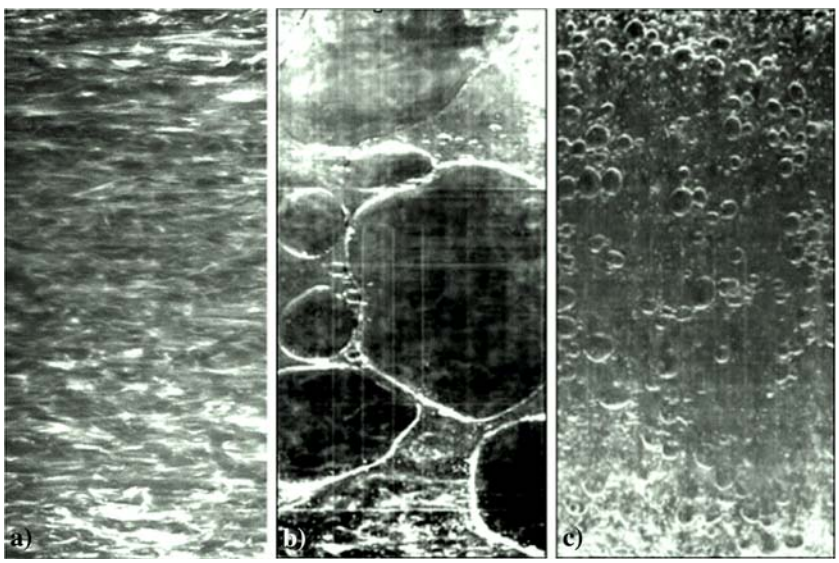

Fig. 3 Near wall turbulence visualized by Kalliroscope. Image frame size is 100 mm × 30 mm. **a** Without bubble, **b** with bubbles larger than 20 mm, **c** with bubbles smaller than 5 mm

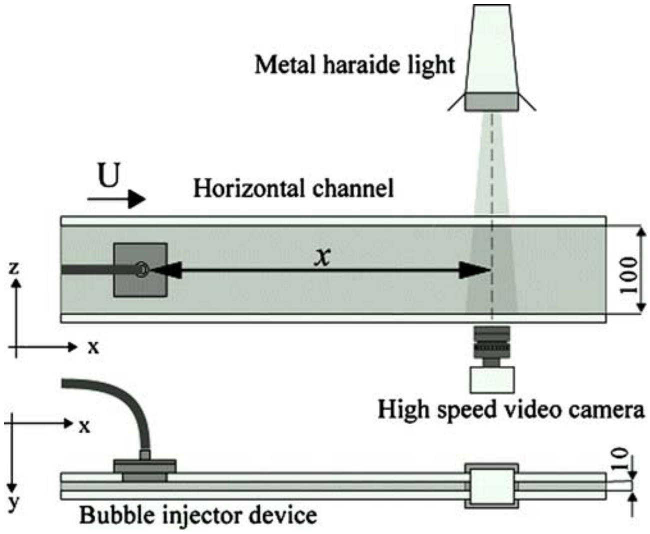

Fig. 4 Schematic of the flow visualization system for PTV measurement

and the depth of field for the particle is kept shallow. To be more precise, we implemented shallow focus imaging to measure the two-dimensional velocity components in a nearly planer space. Figure 5 shows the theoretical depth of field in the case of present particles as a function of the *F* number of the camera. The *F* number is set at 5.6 in this study because of the required distance from the lens to the central plane, and thereby the theoretical depth is around 0.7 mm. Particles suspended in the out-of-focal plane are not projected in the camera, but those in a near-focal plane appear as blurry dark spots. Such unclear particles are removed by a high-pass filter and a binarization of the image to detect individual centroids. We confirmed that the theoretical value of the depth of field coincided with the substantial one measured by a DOF-diagram gauge (Edmund Industrial Optics, DOF 5-15 Depth of Field Target). The image acquisition is carried out using a high-speed digital video camera (Photron FastCam-MAX-120 KC, 1,024 × 1,024 pixels) with a telecentric lens (Computar, TEC-55). The frame rate is 4,000 fps, and the shutter speed is 1/150,000 s. The images are saved to PC memory as digital raw image data format. The field of view for PTV is approximately 12 × 12 mm and the magnification factor is 22.5 μm/pixel. As an analytical algorithm of PTV, we employed the four-step particle tracking method that is known to be good at capturing turbulence (Nishino et al. 1989). Since the time serial images photographed by continuous light are recorded with an equal time interval, being different from double pulse illumination, the four-step particle tracking functions well.

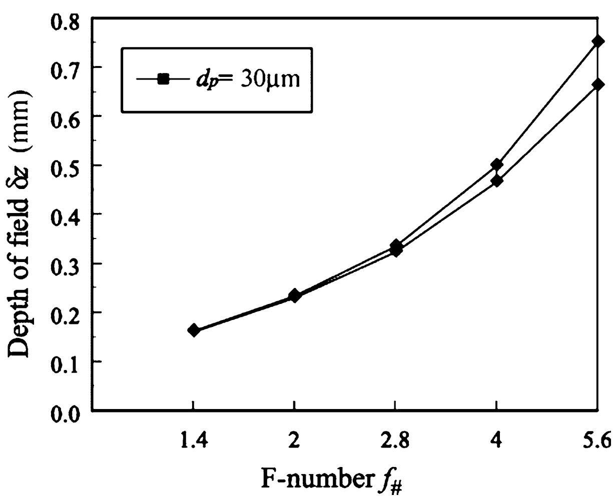

Fig. 5 Relationship between depth of field and *F*-number of camera lens

Figure 6a shows a sample of the original images obtained by the above-mentioned method. Blunt particles and clearly focusing particles co-exist in the original image. Figure 6b shows the high-pass filtered image in which out-of-focus particles are eliminated because of their long wavelength in the spatial brightness distribution. The high-pass filter is a combination of two-dimensional FFT (fast Fourier transform) of the image and the inverse FFT that passes the high wavenumber component. The cutoff wavelength is chosen at 30 μm (3 pixel) according to the particle size. This filtering process also enhances the bubble interface and eliminates the long-wavelength variation of background image, as seen in the figure. Measurement of local void fraction is separately performed using the image, which is binarized and median-filtered from the original image as shown in Fig. 6c.

3 Results and discussion

3.1 Bubble behavior in the channel

The mean void fraction profile across the channel height measured at $x/h = 50$ is shown in Fig. 7. The void fraction is defined by the ratio of a bubble-occupying area to the measurement area on the image, i.e. projection void fraction. This quantity always has a much higher value than three-dimensional void fraction, but can be an alternative variable expressing a bubble's population. In the figure, $y/h = 0$ corresponds to the upper wall surface, and $y/h = 2.0$ the lower wall surface. The local projection void fraction takes the highest value at $y/h = 0.2$, while it is nearly 0 in the lower half region of the channel. Almost the same profile is obtained at $x/h = 800$ as well, implying that the bubble's diffusion and buoyancy effects reach an equilibrium soon after the bubble's injection. The physical reason on the peak-appearing position will be discussed in Sect. 3.3. It is noted that the root-mean-square value of the fluctuation of the local void fraction obeys the

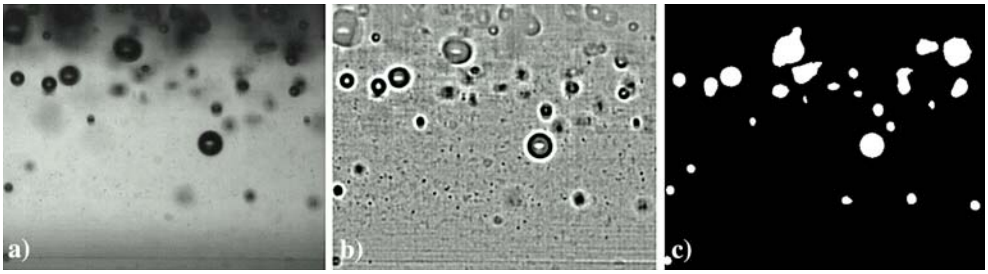

Fig. 6 Image processing to obtain particles' velocity vectors. **a** Original image, **b** high-pass filtered image, **c** separated bubbles

following equation regardless of the bubble motion when the local void fraction is measured with a sufficiently small control volume:

$$\alpha'_{\mathrm{rms}} = \left\{ \frac{1}{T} \int_0^T (\alpha - \bar{\alpha})^2 \mathrm{d}t \right\}^{1/2} = \sqrt{\bar{\alpha}(1-\bar{\alpha})} \quad (1)$$

This relationship stands because the instantaneous void fraction in an infinitely small volume takes the value of 1 or 0. Namely, the deviation of the local void fraction depends only on the average void fraction, and so itself is physically meaningless while its correlation to the velocity fluctuation will show an important role in drag reduction as mentioned in Sect. 3.2.

The number density histogram of the bubble diameter measured at $x/h = 50$ is shown in Fig. 8. The peak-taking bubble diameter is 0.5 mm, and the mean diameter is 0.7 mm. There are no bubbles smaller than 0.3 mm (ref: tracer particle size is 0.03 mm); hence bubbles and particles have been simply distinguished by their sizes during image processing. The largest bubble involved in the histogram is 1.5 mm, which corresponds to 100 in Weber number (We $= \rho U^2 d/\sigma$; ρ is density of liquid, U is bulk mean velocity of liquid, d is bubble diameter, σ is surface tension), and implies a certain bubble deformation.

Figure 9 shows the mean velocity profiles of liquid and bubbles in the top half coordinate of the channel. The graph is normalized by $u_{\max}$, which is the maximum velocity of the liquid phase at the center of the channel. The mean liquid velocity profile follows approximately the 1/7th power law of a single-phase turbulent flow whose profile is indicated by a solid curve. Also, a bubble has a streamwise velocity slightly slower than the liquid velocity near the upper wall surface, or $y/h < 0.4$. This backward slip velocity is about 10–20% of local liquid velocity.

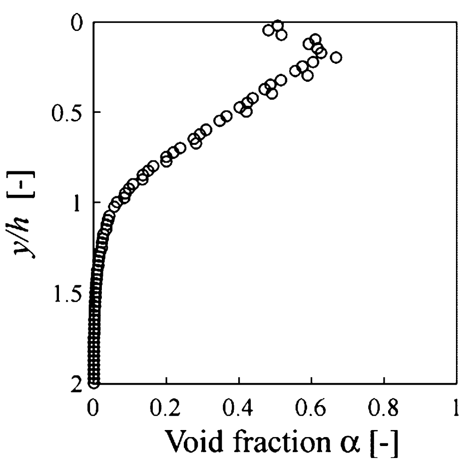

Fig. 7 Projection void fraction profile in the vertical direction

3.2 Turbulent shear stress profile

Reynolds shear stress is one of the most important quantities for evaluating the modification of frictional drag reduction. In the past studies, the introduction of microbubbles and polymers led to a considerable reduction of Reynolds shear stress as actually measured by PIV for microbubbles (Kitagawa et al. 2005), and for polymers (Li et al. 2005). It is known that reduction of the Reynolds shear stress, especially near the wall, can induce highly effective drag reduction as theoretically derived by Fukagata et al. (2002). In this paper, a new type of data analysis is implemented to assess the role of bubble–turbulence interaction in drag reduction. We apply the Reynolds averaging for grid-averaged equation of two-phase momentum conservation, as derived below.

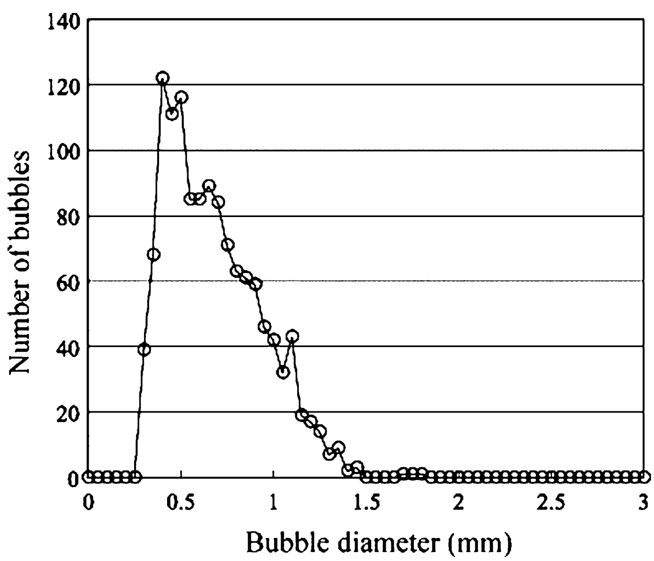

Fig. 8 Number density histogram of bubble diameter

The momentum conservation equations for a two-phase flow as known by the two-fluid model are

$$\frac{\partial f_L \rho_L \mathbf{u}_L}{\partial t} + \nabla \cdot f_L \rho_L \mathbf{u}_L \mathbf{u}_L = -f_L \nabla p + M_{LL} + M_{GL}, \quad (2)$$

$$\frac{\partial f_G \rho_G \mathbf{u}_G}{\partial t} + \nabla \cdot f_G \rho_G \mathbf{u}_G \mathbf{u}_G = -f_G \nabla p + M_{GG} + M_{LG} \quad (3)$$

where suffix L and G denote liquid and gas phases. The local time-dependent variables f, $\mathbf{u}$, p are liquid volume fraction, velocity vector, and pressure. The above two equations adopt a mono-pressure model because the bubble's volumetric pulsation is ignored. The terms M_{LL} and M_{GG} are the inner phase momentum transport, which is modeled in the case of bubbly flow as below:

$$M_{LL} + M_{GG} = \nabla \cdot \mu \left\{ \nabla \mathbf{u}_L + (\nabla \mathbf{u}_L)^T - \frac{2}{3}(\nabla \cdot \mathbf{u}_L) \right\} + f_L \rho_L \mathbf{g} \quad (4)$$

where μ and $\mathbf{g}$ are effective viscosity and the acceleration vector of gravity. The terms M_{GL} and M_{LG} are mutual phase momentum transport (which includes drag, lift, inertia, added inertia, and history force) in the case of bubble. These two terms have the following relationship according to Newton's third law:

$$M_{GL} + M_{LG} = 0. \quad (5)$$

Taking sum of Eqs. 1 and 2, the equation of total momentum conservation is described by

$$\frac{\partial}{\partial t}(f_L \rho_L \mathbf{u}_L + f_G \rho_G \mathbf{u}_G) + \nabla \cdot (f_L \rho_L \mathbf{u}_L \mathbf{u}_L + f_G \rho_G \mathbf{u}_G \mathbf{u}_G) = -\nabla p + \nabla \cdot \mu \left\{ \nabla \mathbf{u}_L + (\nabla \mathbf{u}_L)^T - \frac{2}{3}(\nabla \cdot \mathbf{u}_L) \right\} + f_L \rho_L \mathbf{g}. \quad (6)$$

Since the density of gas is much less than that of a liquid, the net momentum of gas phase is ignorable; hence,

$$\frac{\partial f_L \rho_L \mathbf{u}_L}{\partial t} + \nabla \cdot f_L \rho_L \mathbf{u}_L \mathbf{u}_L = -\nabla p + \nabla \cdot \mu \left\{ \nabla \mathbf{u}_L + (\nabla \mathbf{u}_L)^T - \frac{2}{3}(\nabla \cdot \mathbf{u}_L) \right\} + f_L \rho_L \mathbf{g}. \quad (7)$$

Treating the liquid phase as incompressible fluid and assuming the constant viscosity yield

$$\frac{\partial f_L \mathbf{u}_L}{\partial t} + \nabla \cdot f_L \mathbf{u}_L \mathbf{u}_L = -\frac{1}{\rho_L} \nabla p + \nu \nabla^2 \mathbf{u}_L + f_L \mathbf{g}. \quad (8)$$

This type of a momentum conservation equation for dispersed bubbly flow is employed by Murai and Matsumoto (2000), and Kitagawa et al. (2001). Focusing on streamwise (horizontal) flow, the momentum conservation equation expressed by componential velocity is described by

$$\frac{\partial fu}{\partial t} + \frac{\partial fuu}{\partial x} + \frac{\partial fuv}{\partial y} + \frac{\partial fuw}{\partial z} = -\frac{1}{\rho}\frac{\partial p}{\partial x} + \nu \left(\frac{\partial^2 u}{\partial x^2} + \frac{\partial^2 u}{\partial y^2} + \frac{\partial^2 u}{\partial z^2} \right) \quad (9)$$

Here suffix L is omitted because no gas phase variable remains. The following variable separation into time-average and fluctuation components is carried.

$$\begin{cases} f = \bar{f} + f' \\ u = \bar{u} + u' \\ v = \bar{v} + v' \\ w = \bar{w} + w', \end{cases} \quad (10)$$

where u, v, and w stand for the streamwise velocity, vertical velocity, and spanwise velocity. By substituting these equations into Eq. 9 and averaging overall time, the following equation is obtained:

$$\frac{\partial}{\partial x}\left(\bar{f}\bar{u}\bar{u} + \bar{f}\overline{u'u'} + 2\overline{f'u'}\bar{u} + \overline{f'u'u'} \right) + \frac{\partial}{\partial y}\left(\bar{f}\bar{u}\bar{v} + \bar{f}\overline{u'v'} + \overline{f'v'}\bar{u} + \overline{f'u'}\bar{v} + \overline{f'u'v'} \right) + \frac{\partial}{\partial z}\left(\bar{f}\bar{u}\bar{w} + \bar{f}\overline{u'w'} + \overline{f'w'}\bar{u} + \overline{f'u'}\bar{w} + + \overline{f'u'w'} \right) = -\frac{1}{\rho}\frac{\partial \bar{p}}{\partial x} + \nu \left(\frac{\partial^2 \bar{u}}{\partial x^2} + \frac{\partial^2 \bar{u}}{\partial y^2} + \frac{\partial^2 \bar{u}}{\partial z^2} \right). \quad (11)$$

In a well-developed channel flow, there is no mean vertical velocity and no mean spanwise velocity. The gradient of momentum in the streamwise and spanwise directions is also negligible; therefore,

$$\frac{\partial}{\partial y}\left(\bar{f}\overline{u'v'} + \overline{f'v'}\bar{u} + \overline{f'u'v'} \right) = -\frac{1}{\rho}\frac{\partial \bar{p}}{\partial x} + \nu \frac{\partial^2 \bar{u}}{\partial y^2} \quad (12)$$

This equation is rewritten by

$$\frac{\partial \bar{p}}{\partial x} = \frac{\partial}{\partial y}\left(\mu \frac{\partial \bar{u}}{\partial y} - \rho \bar{f}\overline{u'v'} - \rho \overline{f'v'}\bar{u} - \rho \overline{f'u'v'} \right). \quad (13)$$

Eventually the turbulent shear stress in the case of bubby flow consists of three terms as follows:

$$\tau_1 = -\rho \overline{(1-\alpha)}\overline{u'v'}, \quad (14)$$

$$\tau_2 = \rho \overline{\alpha' v'}\bar{u}, \quad (15)$$

$$\tau_3 = \rho \overline{\alpha' u' v'}, \quad (16)$$

where α stands for local void fraction and $\alpha' = -f'$ is used. The stress component τ_1 is known as Reynolds shear stress, whose absolute value is always reduced by mixing bubbles because of the factor (1 - α). The stress components τ_2 and τ_3 are added components as a two-phase correlation. Using the PTV data, the sign and the magnitude of these three stress components can be obtained quantitatively. It is worth noting that these terms depend on the sampling grid size by which the local void

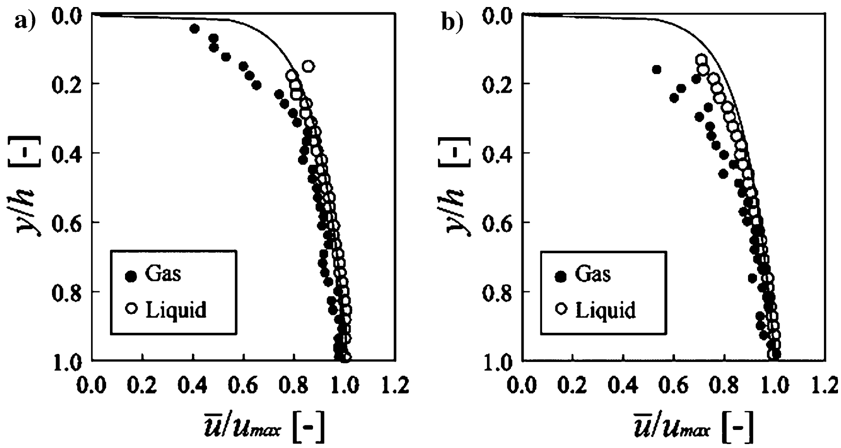

Fig. 9 Mean velocity profiles of two-phase flow. **a** $x/h = 50$, **b** $x/h = 800$

fraction is defined. When a large grid is used, the fluctuation of the void fraction is naturally reduced owing to the averaging effect. When a small grid is used, the fluctuation expands, but its maximum value never diverges to infinity but is restricted to $1 - \bar{\alpha}$ or $\bar{\alpha}$. Therefore, employment of a small grid does not cause unusual errors of measurement.

Figure 10 shows the computed results of the three components of turbulent shear stress, measured at two positions along the flow. The shear stress along the abscissa is normalized by wall shear stress of the single-phase condition τ_w. These results suggest that there is a certain organized interaction between two phases in the bubbly layer of the channel. The following points can be derived from the results. (1) The Reynolds shear stress τ_1 is significantly reduced in the upper half of the channel, as reported by a number of studies. (2) The stress component τ_2 takes a negative value in the upper half at $x/h = 50$. This component originates from the fluctuation correlation between the local void fraction and the vertical liquid velocity as shown by Eq. 15. The magnitude of τ_2 is amplified by the mean flow velocity; therefore, a small correlation will provide a large modification of the local turbulent shear stress. The same trend is confirmed at position $x/h = 800$, but its peak value shifts toward the upper wall surface. (3) The stress component τ_3 takes a small positive value near the upper half of the channel. This component arises as triple correlation among u', v', and α'. Since the correlation u' v' takes a negative value in the upper half of the channel (see Eq. 14), the positive value of τ_3 implies that bubbles avoid tracing a flow event which produces turbulent shear stress. In other words, bubbles do not migrate together in ejection and sweep events.

In terms of the three stress components explained above, the following features of the data analysis must be mentioned. First of all, the data shown here are computed based on the projection void fraction. Therefore, the actual magnitude of correlation including α' will be less than the data shown here. It is roughly estimated at 1/10th. Owing to the restricted availability of optical measurements (such as bubble's overlapping

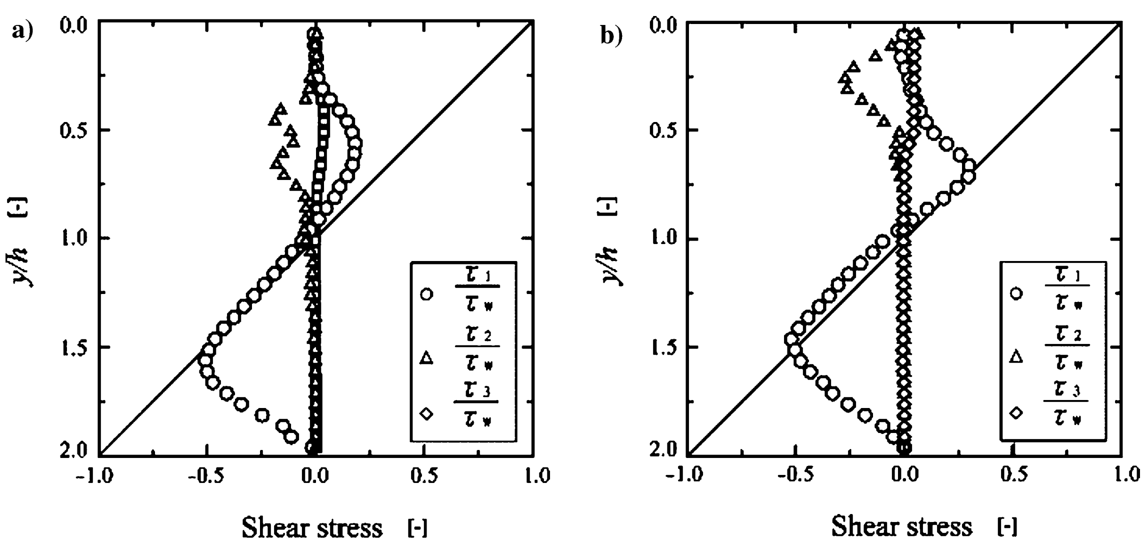

Fig. 10 Turbulent shear stress profiles obtained by PTV data. **a** $x/h = 50$, **b** $x/h = 800$

and deformation), the local profile of three-dimensional void fraction could not be measured. Secondly, the magnitude of the stress depends on the grid size employed. The grid size was 0.11×0.11 mm on the image plane (x–y plane) in this study, which was around 1/5th the typical bubble diameter. We have confirmed that the magnitude was reduced in inverse proportion to the area as two different grid sizes were examined. If the gird size were taken much larger than the bubble size, the fluctuation of the local void fraction would converge onto zero and then the local organized structure expressed by their correlation could not be evaluated. Summarizing the above characteristics of the data analysis, the present data have shown qualitative findings, though the data are quantitative based on chosen sampling conditions. More exact, quantitative evaluation of the componential stress is positioned as our future work.

3.3 On the negative shear stress component

One of the most interesting results derived in this paper is the production of a negative turbulent shear stress component in τ_2. If this component were increased, it would be estimated to result in a more effective drag reduction. In this section, the mechanism of the negative shear stress production is discussed.

According to the definition of τ_2, the following two events provide the negative correlation since the streamwise velocity is positive. Here, the sign of the vertical velocity v is defined as positive when the flow goes upward:

$$(\alpha' > 0) \cap (v' < 0), \tag{17}$$

$$(\alpha' < 0) \cap (v' > 0). \tag{18}$$

The event defined by Eq. 17 means that bubbles concentrate in the region of local downward liquid flow. This type of phenomenon can be called a bubble-repelling event. The event defined by Eq. 18 describes the phenomenon that bubble-free fluid goes up toward the upper wall. This type can be called a liquid sweep event. As the bubble concentration in the vertical direction reaches an equilibrium state, the bubble's repelling from the wall and rising toward the wall must be balanced. This makes us envisage that the bubble-repelling event is locally or suddenly, and the bubble-rising event is slowly, accompanied by a long wavelength in the flow direction. Watching the video images carefully, the upward and downward motions of bubbles as shown in Fig. 11 are quite often observed. The figure shows consecutive images of bubble shadows in the upper half of the channel. Figure 11a shows slowly rising bubbles (as focus, see a circle-marked bubble), while Fig. 11b shows suddenly repelling bubbles from the wall. The vertical rise velocity is around 5% of the streamwise velocity, and deforms as it displaces in the vertical direction because of a sudden change in the velocity gradient. The bubble starts suddenly displacing downward after reaching the nearest point to the wall surface. The downward velocity is around 25% of the streamwise velocity. Consequently, this bubble oscillates in the vertical direction and the oscillation probably produces vertical velocity fluctuation of the liquid phase around the bubble.

In terms of bubbles' accumulation into local downward liquid flow, Mazzitelli et al. (2003) analyzed about it with isotropic turbulence. Their finding was that the action of lift force organized so-called preferential concentration to result in reduced average rise velocity of buoyant bubbles. In the case of turbulent channel flow, the bubble's response to the local downward flow realizes with a high shear rate existing as the background while the lift force plays a major role as well. As shown in Fig. 9, bubbles in this channel have a backward slip velocity in the streamwise direction. Therefore, spherical bubbles receive a downward lift force under the steady shear rate inside the boundary layer. Since the downward lift force ceases in the central channel, there is a balancing point with the upward buoyant force in the boundary layer. A significant inertia force lies between these forces to cause periodic vertical motion of bubbles. Unfortunately, the statistics of such a motion could not be obtained experimentally due to optical limitation as well as the fact that the oscillation wavelength exceeds the photographing window size. Hence, in order to estimate theoretically the amplitude and the frequency of the bubble's oscillation, the following equation of bubble's translational motion is used to compute the trajectory of single bubble in the channel.

$$\beta\rho_L V_G \frac{d\mathbf{u}_G}{dt} + \frac{1}{8}C_D\rho_L\pi d^2|\mathbf{u}_G - \mathbf{u}_L|(\mathbf{u}_G - \mathbf{u}_L) + \frac{1}{2}\rho_L V_G(\mathbf{u}_G - \mathbf{u}_L)\times(\nabla\times\mathbf{u}_L) - \rho_L V_G\mathbf{g} = 0, \tag{19}$$

$$V_G = \frac{1}{6}\pi d^3, \quad C_D = \frac{24}{Re_b}, \quad Re_b = \frac{d|\mathbf{u}_G - \mathbf{u}_L|}{\nu_L}. \tag{20}$$

We consider added inertia, drag, lift, and buoyancy where β is added mass coefficient (= 1/2), C_D is drag coefficient, V_G is volume of single bubble, and d is bubble diameter. In Eq. 19, the liquid flow velocity vector $\mathbf{u}_L$ is given by single-phase steady turbulent flow profile known by the 1/7th power law; hence, its acceleration term does not appear. As the boundary condition of bubbles at the wall, additional friction is taken into account, which acts in the reverse direction to the flow. The friction is modeled by bubble velocity ratio, i.e. the bubble velocity relative to the liquid velocity at the interfacial contact condition. According to the experimental observation, the velocity ratio is estimated as 0.1 in this study, and this value roughly matches the work done by Masliyah et al. (1994) and Moctezuma et al. (2005) for an inclined and vertical wall.

Figure 12 shows three kinds of bubble trajectory dependent on the bubble diameter d. The trajectory is computed under the present experimental conditions. The bubble starting from zero-velocity near the upper

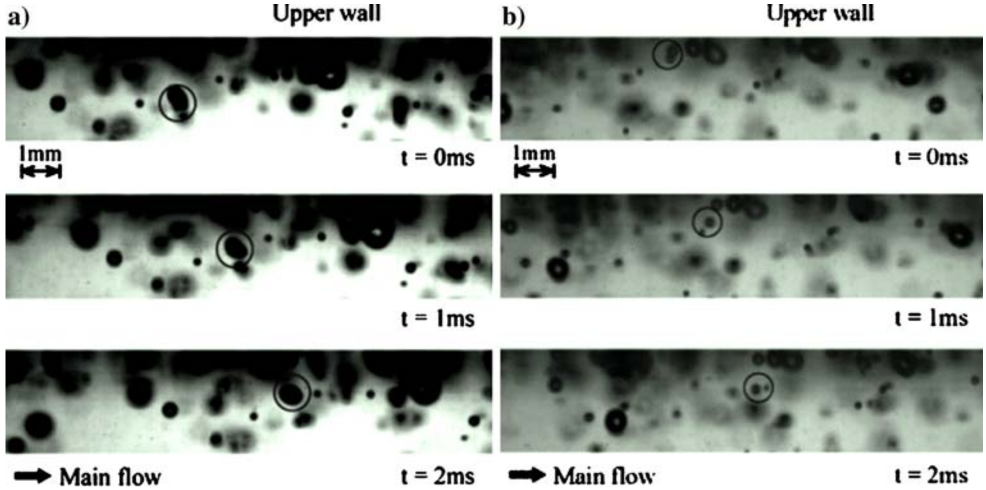

Fig. 11 Motion of bubbles in the vicinity of the upper wall. **a** Rising bubble, **b** descending bubble

wall initially goes down due to the lift force (third term in Eq. 19), and accelerates in the streamwise direction with drag force (second term in Eq. 19). It subsequently reaches the lowest location at which the buoyancy (fourth term in Eq. 19) exceeds the lift. The lowest location depends on the bubble's diameter. Next, the bubble slowly rises and experiences slow liquid velocity near the wall that suddenly reduces its streamwise velocity. When the bubble interface contacts with the wall, the streamwise bubble velocity suddenly decelerates and generates the downward lift force again. Repeating this cycle, a bubble of d = 0.3 mm shows a vertical oscillation at 23 Hz, d = 0.5 mm at 17 Hz, and d = 1.0 mm at 14 Hz. It is noted that the frequency changed within 10% as the bubble velocity ratio on the wall varied from 0.0 to 0.8 while no bouncing phenomena occurs in the case of the bubble velocity ratio higher than 0.8. The experimental observation of bubble's oscillation is roughly from 10 to 20 Hz, and corresponds well to the computed value. Thus, the bubble-repelling event defined by Eq. 17 is explained by the relative motion of a bubble to the liquid in the shear layer. Simultaneously, this bubble trajectory simulation confirms the existence of a mean backward slip velocity

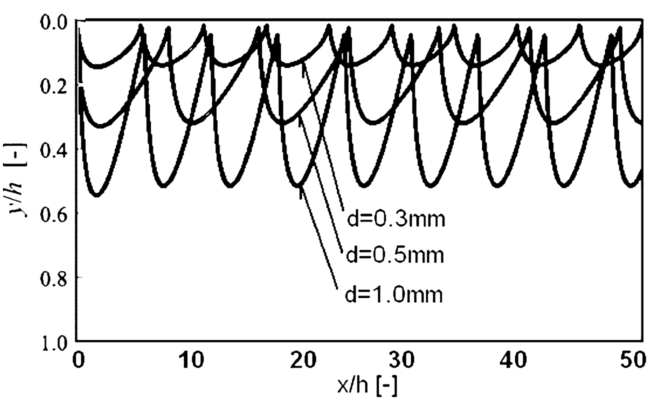

Fig. 12 Motion of bubbles simulated by bubble's translational motion equation

of bubbles, whose experimental data are shown in Fig. 9. That is, the bubbles, which separate suddenly from the near wall region, have a velocity slower than the liquid, owing to the added inertia effect. Drag is apparently only a secondary force to follow the liquid at the bubble-repelling event.

The discussion at the present stage goes no further than finding the source of the negative shear stress component, and we need to clarify more detailed relationship between the measurement results of τ_2 and the analytical results of bubble trajectories in the next phase. Anyhow, such a phenomenon is one of the particular characteristics of the drag reduction using an "intermediate size" bubble. Namely, it is strongly associated with the bubble's relative motion to liquid while a microbubble does not show such an oscillatory motion because of no allowed slip due to viscosity. We think that there is an intrinsic role of drag reduction in using such intermediate bubbles which are much more feasible for engineering applications.

4 Conclusion

In this study, a series of experiments and some theoretical considerations are carried out to discuss the modification of turbulent shear stress in a horizontal bubbly channel flow. Three kinds of turbulent shear stress terms are derived and measured using PTV. The results have shown that the triple correlation term $\alpha' u' v'$ has a small positive stress, and the correlation $\alpha' v'$ has a negative stress in the bubbly two-phase layer. The former fact indicates that bubbles do not actively follow the local stress-producing events such as ejection and sweep. The latter fact indicates the possibility of promoting drag reduction using intermediate-sized (non-microbubble) bubbles. The origin of the negative shear stress production, which was ascertained by experimental observations and theoretical estimations, is a bubble's repelling event that is induced by the downward-acting lift force in the near-wall region. The bubble trajectory simulation has confirmed the experimental finding, and also explored the feature of bubble's cyclic oscillation, which is one of the particular phenomena generating the drag reduction in the case of an intermediate bubble size.

Acknowledgments The authors of this paper are grateful for the support of the Office of Naval Research under grant N00014-03-1-0299 (Dr. L. Patrick Purtell), and also to the National Maritime Research Institute of Japan (Dr. Y. Kodama). A part of the study was also supported by Grant-aided scientific research of the Japanese Ministry of Education & Science (MEXT): No.17686014. In addition, there were helpful discussions in the microbubble drag reduction community (Prof. K. Hishida, Prof. Kato, Dr. K. Sugiyama, Dr. T. Kawamura, and Dr. A. Kitagawa) in preparation of this paper.

References

Dominguez-Lerma MA, Ahlers G, Channell DS (1985) Effects of Kalliroscope flow visualization particles on rotating Couette-Taylor flow. Phys Fluids 28:1204–1206

Felton K, Loth E (2002) Diffusion of spherical bubbles in a turbulent boundary layer. Int J Multiphase Flow 28:69–92

Ferrante A, Elghobashi S (2004) On the physical mechanism of drag reduction in a spatially developing turbulent boundary layer laden with microbubbles. J Fluid Mech 503:345–355

Fukagata K, Iwamoto K, Kasagi N (2002) Contribution of Reynolds stress distribution to the skin friction in wall-bounded flows. Phys Fluids 14:L73–L76

Fukuda K, Tokunaga J, Nobunaga T, Nakatani T, Iwasaki T (2000) Frictional drag reduction with air lubricant over a super-water-repellent surface. J Mar Sci Tech 5:123–130

Fukuda H, Oishi Y, Murai Y, Kodama Y, Yamamoto F (2005) Modification of skin frictional drag of gas-liquid two-phase flow in a horizontal channel. In: Proceedings of the 2nd international symposium on seawater drag reduction, pp 125–133

Gabillet C, Colin C, Fabre J (2002) Experimental study of bubble injection in a turbulent boundary layer. Int J Multiphase Flow 28:553–578

Kato H, Iwashina T, Miyanaga M, Yamaguchi H (1999) Effect of microbubbles on the structure of turbulence in a turbulent boundary layer. J Mar Sci Tech 4:115–162

Kawamura T, Kodama Y (2002) Numerical simulation method to resolve interactions between bubbles and turbulence. Int J Heat Fluid Flow 23:627–638

Kitagawa A, Murai Y, Yamamoto F (2001) Two-way coupling of Eulerian-Lagrangian model for dispersed multiphase flows using filtering functions. Int J Multiphase Flow 27:2129–2153

Kitagawa A, Hishida K, Kodama Y (2005) Flow structure of microbubble-laden turbulent channel flow measured by PIV combined with the shadow image technique. Exp Fluids 38:466–475

Kodama Y, Kakugawa A, Takahashi T, Kawashima H (2000) Experimental study on microbubbles and their applicability to ships for skin friction reduction. Int J Heat Fluid Flow 21:582–588

Latorre R, Miller A, Philips R (2003) Micro-bubble resistance reduction on a model SES catamaran. Ocean Eng 30:2297–2309

Legner HH (1984) Simple model for gas bubble drag reduction. Phys Fluids 27:2788–2790

Li FC, Kawaguchi Y, Segawa T (2005) Reynolds-number dependence of turbulence structures in a drag-reducing surfactant solution channel flow investigated by particle image velocimetry. Phys Fluids 17:1–13

Lu J, Fernandez A, Tryggvason G (2005) The effect of bubbles on the wall drag in a turbulent channel flow. Phys Fluids 17:1–12

Madavan NK, Deutsch S, Merkle CL (1985) Measurements of local skin friction in microbubble-modified turbulent boundary layer. J Fluid Mech 156:237–256

Marie JL (1987) A simple analytical formulation for microbubble drag reduction. J Phys Chem Hydro 13:213–220

Masliyah J, Jauhari R, Gray M (1994) Drag coefficient for air bubbles rising along an inclined surface. Chem Eng Sci 49:1905–1911

Mazzetelli IM, Lohse D, Toschi F (2003) On the relevance of the lift force in bubbly turbulence. J Fluid Mech 488:283–313

McCormick M, Bhattacharyya R (1973) Drag reduction of a submersible hull by electrolysis. Nav Eng J 85:11–16

Merkle CL, Deutsch S (1992) Microbubble drag reduction in liquid turbulent boundary layers. ASME Appl Mech Rev 45:103–127

Moctezuma MF, Lima-Ochoterena R, Zenit R (2005) Velocity fluctuations resulting from the interaction of a bubble with vertical wall. Phys Fluids 17:1–4

Moriguchi Y, Kato H (2002) Influence of microbubble diameter and distribution on frictional resistance reduction. J Mar Sci Tech 7:79–85

Murai Y, Matsumoto Y (2000) Numerical study of the three-dimensional structure of a bubble plume. J Fluids Eng Trans ASME 122:754–760

Nishino K, Kasagi N, Hirata M (1989) Three dimensional particle tracking velocimetry based on automatic digital image processing. J Fluids Eng ASME 111:384–391

Takahashi T, Kakugawa A, Makino M., Kodama Y (2003) Experimental study on scale effect of drag reduction by microbubbles using very large flat plate ships. J Kansai Soc N A Japan 239:11–20

Xu J, Maxey ML, Karniadakis GE (2002) Numerical simulation of turbulent drag reduction using micro-bubbles. J Fluid Mech 468:271–281